

## Thermodynamic Scaling of the Hydrological Cycle of the Last Glacial Maximum

WILLIAM R. BOOS

*Department of Geology and Geophysics, Yale University, New Haven, Connecticut*

(Manuscript received 4 January 2011, in final form 1 September 2011)

### ABSTRACT

In climate models subject to greenhouse gas–induced warming, vertically integrated water vapor increases at nearly the same rate as its saturation value. Previous studies showed that this increase dominates circulation changes in climate models, so that precipitation minus evaporation ( $P - E$ ) decreases in the subtropics and increases in the tropics and high latitudes at a rate consistent with a Clausius–Clapeyron scaling. This study examines whether the same thermodynamic scaling describes differences in the hydrological cycle between modern times and the last glacial maximum (LGM), as simulated by a suite of coupled ocean–atmosphere models. In these models, changes in water vapor between modern and LGM climates do scale with temperature according to Clausius–Clapeyron, but this thermodynamic scaling provides a poorer description of the changes in  $P - E$ . While the scaling is qualitatively consistent with simulations in the zonal mean, predicting higher  $P - E$  in the subtropics and lower  $P - E$  in the tropics and high latitudes, it fails to account for high-amplitude zonal asymmetries. Large horizontal gradients of temperature change, which are often neglected when applying the scaling to next-century warming, are shown to be important in large parts of the extratropics. However, even with this correction the thermodynamic scaling provides a poor quantitative fit to the simulations. This suggests that circulation changes play a dominant role in regional hydrological change between modern and LGM climates. Changes in transient eddy moisture transports are shown to be particularly important, even in the deep tropics. Implications for the selection and interpretation of climate proxies are discussed.

### 1. Introduction

Earth's hydrological cycle is projected to change over the next century in response to increased greenhouse gas concentrations, exhibiting enhanced tropical precipitation, reduced subtropical precipitation, and an increase in global-mean precipitable water (Meehl et al. 2007). This response is consistently exhibited across a suite of coupled ocean–atmosphere models, and although these models use numerous complex and uncertain representations of subgrid-scale physics, there are fundamental reasons to expect such a response. The atmospheric boundary layer contains the bulk of column-integrated atmospheric water, and boundary layer specific humidity over oceans, which cover most of earth's surface, is constrained by the surface energy balance to increase with temperature approximately following the Clausius–Clapeyron relation (Held and Soden 2000;

Boer 1993).<sup>1</sup> If changes in the general circulation of the atmosphere are relatively small, as they seem to be in climate models, then a spatially uniform increase in precipitable water will enhance the existing pattern of precipitation minus evaporation ( $P - E$ ), increasing  $P - E$  in the tropics and high latitudes and decreasing it in the subtropics as climate warms (Held and Soden 2006; Chou and Neelin 2004; Seager et al. 2010; Kutzbach et al. 2005; Emori and Brown 2005).

Although climate models consistently predict these patterns of coming hydrological change, consistency is no guarantee of correctness and there are, of course, no observations of future climate to constrain the models. An alternate approach to testing theory and models looks to the past. The climate of the last glacial maximum

Corresponding author address: William R. Boos, Department of Geology and Geophysics, Yale University, P.O. Box 208109, New Haven, CT 06520-8109.  
E-mail: billboos@alum.mit.edu

<sup>1</sup> In this paper we focus on changes in precipitable water that are dominated by changes in boundary layer humidity. Changes in free-tropospheric humidity, which make a smaller contribution to precipitable water but have a larger influence on the planetary radiative balance, are less well-constrained and are reviewed by Pierrehumbert et al. (2007) and Sherwood et al. (2010b).

(LGM), a period roughly 21 000 years before present, has been simulated by the Paleoclimate Modeling Intercomparison Project (PMIP) using a suite of coupled ocean–atmosphere models forced by reduced greenhouse gas concentrations and imposed large continental ice sheets (Braconnot et al. 2007; Joussaume and Taylor 1995). Relative to modern climate, the LGM is an anomalously cold state rather than a warm one; if theories for hydrological change can be applied to such a cold state then it may be possible to determine whether theory, numerical simulations, and indirect records of past climate (i.e., climate proxies) all agree. Numerous previous studies have compared LGM climate simulations with theory and proxies, but much of the focus has been on changes in surface temperature and the feedback processes that determine those changes (e.g., Broccoli 2000; Yoshimori et al. 2009; Hargreaves et al. 2007; Lainé et al. 2009).

It is clear that the LGM cannot be thought of as a perfect “cold analogue” for next-century warming because LGM continental ice sheets exert an anomalous localized radiative forcing that is nearly as large in the global mean as the forcing due to reduced carbon dioxide; these ice sheets also mechanically perturb the flow (Broccoli and Manabe 1987; Kageyama et al. 1999; Ganopolski et al. 1998; Braconnot et al. 2007; Broccoli 2000). Nevertheless, simulations of LGM climate seem to show some evidence for hydrological change that is qualitatively opposite to that predicted for next-century warming, namely, a reduction in tropical and high-latitude precipitation and an increase in winter precipitation in some subtropical regions, relative to modern climate (Ganopolski et al. 1998; Street-Perrott and Harrison 1985; Winkler and Wang 1993). Furthermore, Ramstein et al. (1998) noted that global-mean precipitation and atmospheric water vapor were lower in LGM simulations than in modern climate and that the local change in precipitable water seemed to have the same sign as the coincident change in sea surface temperature. It has been explicitly suggested that the LGM might serve as a cold climate in which the aforementioned thermodynamic scaling for  $P - E$  can be verified through the use of climate proxies (Quade and Broecker 2009). However, no study has quantitatively examined whether the changes in  $P - E$ , precipitable water, and temperature in LGM climate simulations obey the same thermodynamic scalings seen in simulations of future climate. That is the goal of this paper: to determine whether the theoretical scaling based on the Clausius–Clapeyron relation that seems to govern precipitable water and  $P - E$  in simulations of future climate (e.g., Held and Soden 2006) also holds in simulations of the LGM.

A thermodynamic scaling is only expected to provide an approximate description, at best, of hydrological change because winds are expected to change with global-mean temperature. Model simulations predict a reduction in the strength of the Hadley circulation in next-century warming, as well as a meridional widening of that circulation and an associated poleward shift in the extratropical meridional circulation (e.g., Schneider et al. 2010; Held and Soden 2006). This reduces the poleward moisture flux below that expected based on a Clausius–Clapeyron scaling and extends the poleward boundary of the subtropical dry zones further poleward (Seager et al. 2010). As might then be expected for a colder climate, model simulations show a strengthening and meridional contraction of the LGM Hadley circulation (Rind 1998; Murakami et al. 2008). While such circulation changes are expected to modify the hydrological cycle, we leave an examination of the consistency of LGM changes with theoretical dynamical scalings (e.g., O’Gorman and Schneider 2008) for future work. Here, we focus on the more limited issue of whether a thermodynamic scaling can provide an adequate, first-order description of  $P - E$  during the LGM.

The next section of this paper reviews the theoretical scaling for the hydrological cycle set forth in previous studies and notes some caveats for the LGM. Model simulations analyzed in this study are then described. Subsequent sections present the differences in precipitable water and  $P - E$  between the simulated LGM and modern climates, and these distributions are compared with the thermodynamic scaling. While we do not conduct any direct comparisons with climate proxies, we do discuss the implications of our results for the selection and interpretation of proxies.

## 2. Review of theoretical scalings

We begin by reviewing constraints on precipitable water and  $P - E$  that arise when lower-tropospheric relative humidity does not change as climate warms or cools. Of prime importance is the fact that the relative humidity of the oceanic boundary layer is expected to remain nearly constant given the relatively small changes in surface air temperature that occur between the climates of the LGM, modern, and next-century periods. Oceanic boundary layer relative humidity is constrained by the surface energy balance and by the fact that surface wind speeds are not expected to change dramatically; if boundary layer relative humidity did change substantially then the associated necessary change in surface evaporation would require an implausibly large change in either net surface radiation or air–sea temperature

difference (Held and Soden 2000).<sup>2</sup> Humidity just above the boundary layer does contribute significantly to precipitable water and is not subject to the same constraint, but lower-tropospheric relative humidities also remain relatively constant in climate models. Some theoretical explanations for this behavior exist (Pierrehumbert et al. 2007; Sherwood et al. 2010b).

If humidity remains a fixed fraction of its saturation value, then its variations can be described by an approximate Clausius–Clapeyron relation,

$$\frac{e_2}{e_1} = \exp\left[\frac{L_v}{R_v}\left(\frac{T_2 - T_1}{T_2 T_1}\right)\right], \quad (1)$$

where  $T$  and  $e$  are temperature and saturation water vapor pressure, respectively, with numerical subscripts denoting two different thermodynamic equilibrium states. The latent heat of vaporization is denoted by  $L_v$ , and  $R_v$  is the gas constant for water. This form of the Clausius–Clapeyron relation was obtained by neglecting the specific volume of liquid water compared to that of water vapor and also neglecting the temperature dependence of  $L_v$ . If we further assume that temperature variations  $\Delta T \equiv T_2 - T_1$  are small compared to the absolute temperature  $T_1$ , we obtain the simplified expression

$$\frac{e_2}{e_1} = \exp(\alpha \Delta T). \quad (2)$$

Here,  $\alpha = L_v R_v^{-1} T_1^{-2}$ , which is between 0.06 and 0.09 for lower-tropospheric temperatures in both modern climate and LGM simulations, with values in the upper end of that range typically achieved only over ice. The expression (2) has been used in previous studies of simulated next-century hydrological change (e.g., Held and Soden 2006; Lorenz and DeWeaver 2007) and has an error, relative to the formula for saturation vapor pressure given by Bolton (1980), of less than 1% for  $|\Delta T| \leq 5$  K.

As in previous studies of the scaling of the hydrological cycle in next-century climate change (e.g., Trenberth et al. 2003; Held and Soden 2006), we wish to obtain an expression like (2) that applies to the vertically integrated, mass-weighted water vapor  $W$ . If  $\alpha$ ,  $\Delta T$ , and the relative humidity were constant with height, then (2) could be integrated exactly in the vertical. However,  $\Delta T$  increases in magnitude with height along a moist adiabat,

and relative humidity typically varies strongly with height in the troposphere. Nevertheless, following Lorenz and DeWeaver (2007), we use a similar logarithmic relation for column water vapor,

$$\log\left(\frac{W_2}{W_1}\right) = \bar{\alpha} \Delta T_s, \quad (3)$$

but with  $\bar{\alpha}$  now representing the rate at which precipitable water changes with the surface air temperature  $\Delta T_s$ . We henceforth use  $\bar{\alpha}$  in our notation, retaining the overbar to emphasize that it is an average rate of change weighted by the vertical structures of both humidity and temperature. To avoid some of the ambiguities introduced by these variable vertical structures, we follow O’Gorman and Muller (2010) and compare model-simulated values of  $\bar{\alpha}$  with the values expected for a saturated atmosphere and for an atmosphere in which the seasonal climatology of relative humidity does not change with climate state. We use changes in surface air temperature  $\Delta T_s$  in (3) instead of a mass-weighted lower-tropospheric temperature for consistency with previous studies (e.g., Held and Soden 2006) and because surface air temperature was more widely archived among the models examined here than lower-tropospheric temperatures. Using surface air temperature also eliminates the need to adjust the level at which  $\Delta T$  is evaluated in regions where LGM ice sheets substantially alter topography. Note that we will generally employ (3) to solve for  $\bar{\alpha}$  instead of plotting relative changes in  $W$  against  $\Delta T_s$ , because the logarithm eliminates the need to convert between finite and differential rates of change (see discussion by O’Gorman and Muller 2010).

On climatological time scales, convergence of the vertically integrated moisture flux  $\vec{F}$  is balanced by  $P - E$ :

$$P - E = -\nabla \cdot \vec{F}. \quad (4)$$

Here,  $\vec{F}$  is simply the mass-weighted, vertically integrated water vapor transport:

$$\vec{F} = \frac{1}{g} \int_0^{p_s} \mathbf{v} q \, dp, \quad (5)$$

where  $p_s$  is surface pressure,  $\mathbf{v}$  is the vector horizontal wind, and  $q$  is specific humidity. As discussed in Held and Soden (2006), a simple scaling for  $P - E$  can be obtained if the change in  $\vec{F}$  with temperature is dominated by the change in lower-tropospheric  $q$  assuming fixed relative humidity and fixed winds. Then  $\vec{F}$  scales according to the Clausius–Clapeyron relation so that a linearized estimate of the change in  $P - E$  is

$$\delta(P - E) = -\nabla \cdot (\bar{\alpha} \delta T \vec{F}). \quad (6)$$

<sup>2</sup> Both surface radiation and air–sea temperature difference do change between the LGM and modern climate simulations in the model archive examined here, but these changes are small compared to those needed to effect a boundary layer relative humidity change larger than a few percent (based on a steady state surface energy budget over ocean).

TABLE 1. Characteristics of models used in this study.

Model name	Atmosphere resolution	Dynamic vegetation	Moisture transports reported
Community Climate System Model 3 (CCSM3)	T42, 18 levels	No	No
Centre National de Recherches Météorologiques Coupled Model 3.3 (CNRM-CM3.3)	T42, 31 levels	No	No
ECHAM53 Max Planck Institute Ocean Model (MPI-OM) version 127	T31, 19 levels	No	No
ECHAM53-MPI-OM127, with Lund-Potsdam-Jena (LPJ) vegetation	T31, 19 levels	Yes	No
Flexible Global Ocean-Atmosphere-Land System gridpoint version 1.0 (FGOALS-g1.0)	$2.8^\circ \times 2.8^\circ$ , 26 levels	No	No
Third climate configuration of the Met Office Unified Model, Met Office Surface Exchange System (MOSES II) land surface (HadCM3M2)	$3.75^\circ \times 2.5^\circ$ , 19 levels	No	Yes
L'Institut Pierre-Simon Laplace Coupled Model 4, version 1 medium resolution (IPSL-CM4-V1-MR)	$3.75^\circ \times 2.5^\circ$ , 19 levels	No	No
Model for Interdisciplinary Research on Climate 3.2 (MIROC3.2)	T42, 20 levels	No	Yes

For simulations of next-century warming, it is often assumed that relative horizontal variations in  $\mathbf{F}$  are much larger than relative horizontal variations in  $\delta T$  or  $\bar{\alpha}$ , which allows gradients in the latter quantities to be neglected in the above expression (e.g., Held and Soden 2006). This approximation, however, is not valid in substantial parts of the extratropics when examining changes between modern and LGM climates because of large gradients in  $\delta T$  near ice sheets. Thus, the simplest expression for the thermodynamic scaling of  $P - E$  for this particular application is

$$\delta(P - E) = \bar{\alpha}\delta T(P - E) - \bar{\alpha}\mathbf{F} \cdot \nabla(\delta T). \quad (7)$$

The first term on the right-hand side represents the moisture convergence field simply scaling with temperature, so that wet regions get wetter and dry regions get drier as temperatures rise (where “wet” and “dry” here refer to  $P - E$  and not humidity). The second term, which is often neglected in studies of next-century warming, represents the change in moisture convergence due to spatially inhomogeneous temperature change. This term would account, for example, for enhanced moisture convergence that occurs as winds blow from a region experiencing no temperature change into a region experiencing a large temperature drop. Even the more complete expression in (7) neglects a third term that accounts for horizontal variations in  $\bar{\alpha}$ , but we will show below that this term is quite small in model simulations examined here. A related decomposition is provided by Chou and Neelin (2004), who call the physics represented by the first term on the right-hand side of (7) the “rich-get-richer” mechanism. They also discuss the effect of anomalous horizontal gradients of moisture in their “upped-ante” mechanism.

### 3. Models and methods

#### a. Description of model archive

This study employs output from a suite of coupled ocean-atmosphere models archived by the Paleoclimate

Modeling Intercomparison Project Phase 2 (PMIP2; Braconnot et al. 2007). These models were used to simulate climates of the LGM (21 ka), mid-Holocene (6 ka), and preindustrial (0 ka, roughly A.D. 1750, herein referred to as modern) periods, using a standardized set of forcings and boundary conditions. All models used fully dynamical oceans with interactive sea ice, and a small subset used dynamic vegetation.

Details on model configuration are provided in Braconnot et al. (2007), and we mention only a few points here. Modern integrations used orbital parameters from A.D. 1950 and trace gases estimated for A.D. 1750, including a CO<sub>2</sub> concentration of 280 ppmv. Orbital parameters for all runs were derived from Berger (1978). The LGM integrations used reduced greenhouse gas concentrations resulting in an anomalous tropospheric radiative forcing of  $-2.8 \text{ W m}^{-2}$  relative to modern runs. The ICE-5G ice sheet reconstruction (Peltier 2004) was used in the LGM runs, which specifies an ice sheet that exceeds 3 km in height over North America. Different methodologies were used among the various models to initialize the ocean model to a glacial state.

The models used a range of resolutions, most commonly around T42 and 20 levels for the atmosphere, and  $1.25^\circ \times 1.25^\circ$  and 20 levels for the ocean. Results presented here were taken from 100-yr averages for a period in which each modeling group deemed time trends to be small. We used results from eight models (Table 1) for which output was available for both LGM and modern periods. Vertically integrated moisture fluxes  $\mathbf{F}$  were available for only two of these models, and so the complete thermodynamic contribution to the change in  $P - E$  was calculated only for those models. While  $\mathbf{F}$  was technically available for the Flexible Global Ocean-Atmosphere-Land System Model gridpoint version 1.0 (FGOALS-g1.0), it possessed a high amount of spectral ringing and so was omitted from analyses requiring  $\mathbf{F}$ .

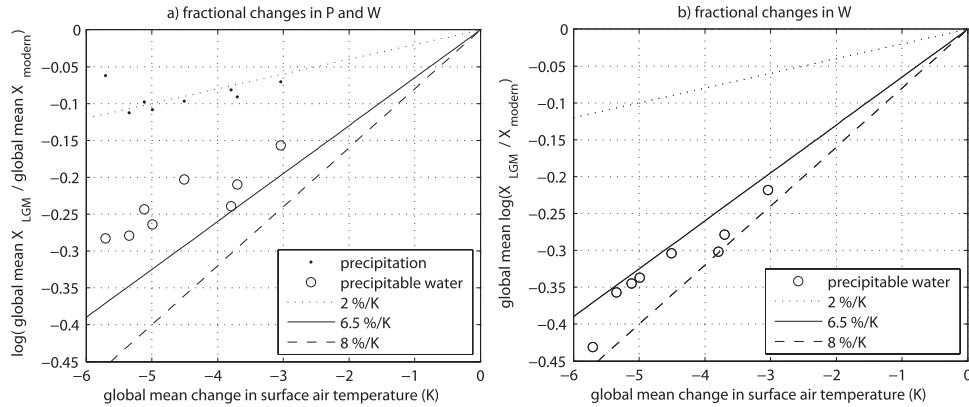


FIG. 1. Change in precipitable water (open circles) and in precipitation (dots), plotted against change in surface air temperature for each model in Table 1. (a) The result computed by taking the global means and then their ratio before the natural logarithm. (b) The result computed by taking the global mean of the logarithm of the ratio at each horizontal grid point. Results for precipitation are shown only in (a) because this avoids division by small numbers in regions where precipitation is locally near zero. Dotted, solid, and dashed lines represent rates of change of 2%, 6.5%, and 8%  $K^{-1}$ .

### b. Analysis methods

All calculations were performed in the archived model resolutions; then plots were made by regridding the results from each model to the same  $128 \times 64$  Gaussian grid on which data was archived for the T42 models. Most calculations of rates of change of vertically integrated water vapor were performed using the precipitable water archived by each modeling group, but rates of change under the assumption of constant relative humidity and under the assumption of a saturated atmosphere (see below) required vertical integration. Such integrals were calculated in a piecewise-linear sense and evaluated exactly from surface pressure to the top of the atmosphere in the pressure coordinate archived for each model. All horizontal gradients were calculated on a sphere using a centered, second-order difference scheme.

### 4. Changes in precipitable water

We first examine how precipitable water  $W$  varies with climate state in the PMIP2 integrations. This examination of changes in  $W$  is a task analogous to that conducted for simulations of the next century by Held and Soden (2006), Boer (1993), Allen and Ingram (2002), and Trenberth et al. (2003). Compared to those studies, our task is complicated by large horizontal inhomogeneities of temperature change between the LGM and modern periods. In other words, the nonlinear nature of (3) makes it matter whether one takes the global mean of  $W$  before or after taking the ratio and logarithm. If, as in Held and Soden (2006), we plot the relative change in global-mean  $W$  against the change in global-mean surface air temperature, the rate of change is about  $5\% K^{-1}$ , considerably

lower than Clausius–Clapeyron rates (Fig. 1a). This occurs because the surface air temperature change between modern and LGM climates is much larger at high latitudes, with more than 30 K of cooling over parts of the Northern Hemisphere ice sheets, compared to a global-mean surface air temperature change of 3–6 K (Fig. 2a, and Braconnot et al. 2007). While polar amplification of temperature change is also seen in simulations of next-century warming, it is more moderate, with warming peaking near 7 K near the north pole for an increase of global-mean surface air temperature near 3 K (Meehl et al. 2007). Some of the surface air temperature change over the Laurentide ice sheet is likely associated with changes in altitude, but since saturation vapor pressure depends only on temperature and not on altitude or surface pressure, the cause of the cooling does not matter for purposes of computing a thermodynamic scaling for  $W$ . Figure 2b shows the quantity  $W_{LGM}/W_{mod}$ , where subscripts denote the LGM and modern climates, respectively. The fractional change in  $W$  indeed exhibits a large degree of inhomogeneity but spatially resembles the temperature change. Taking the global mean of the quantity  $\log(W_{LGM}/W_{mod})$ , calculated for each horizontal point from an annual-mean climatology, shows that all PMIP2 models exhibit a precipitable water scaling between  $6.5\%-8.0\% K^{-1}$  (Fig. 1b), more consistent with a Clausius–Clapeyron scaling.

We have not presented horizontal maps of  $\bar{w}$  because this calculation would involve division by zero since  $\Delta T_s$  changes sign in some regions. Zonal-mean plots of  $\bar{w}$ , however, can be produced by dividing the zonal mean of  $\log(W_{LGM}/W_{mod})$  by zonal-mean  $\Delta T_s$  since the latter is everywhere nonzero in all but one model. That model

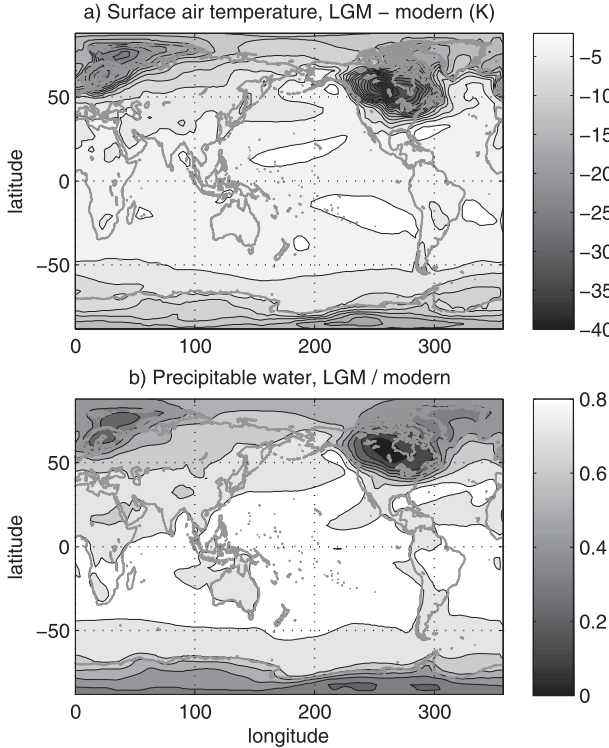


FIG. 2. Multimodel mean of (a) difference between LGM and modern surface air temperature with a contour interval of 2 K and shading starting at -2 K, and (b) ratio of LGM to modern precipitable water with a contour interval of 0.1 and shading starting at 0.8. Plots include data from all eight models in Table 1.

[Centre National de Recherches Météorologiques Coupled Global Climate Model, version 3.3 (CNRM-CM3.3)] is omitted from the calculation because its  $\Delta T_s$  changes sign near 60°S; outside the range of 50°–70°S, this omission makes a negligible difference in the multimodel-mean  $\bar{\alpha}$ . Figure 3 shows this zonal-mean estimate of  $\bar{\alpha}$  and confirms, as was qualitatively inferred from Fig. 2, that the larger cooling over the high-latitude ice sheets is accompanied by a larger reduction in  $W$  in the range expected for a Clausius–Clapeyron scaling. The global and multimodel-mean value of  $\bar{\alpha}$  is  $7.7\% \text{ K}^{-1}$ , but significant meridional variations exist. If  $\bar{\alpha}$  is instead calculated by dividing the zonal mean of  $\log(W_{\text{LGM}}/W_{\text{mod}})$  by the global-mean temperature change, its values become much larger at high latitudes (more than  $15\% \text{ K}^{-1}$ , not shown) simply because  $\Delta T_s$  is so much larger over the high-latitude ice sheets.

By the same methodology used to compute zonal-mean  $\bar{\alpha}$ , we have also computed the rate of change of  $W$  that would occur under the assumption of unchanged relative humidity. That is, the monthly-mean climatology of modern relative humidity at each latitude, longitude, and pressure level was multiplied by the saturation

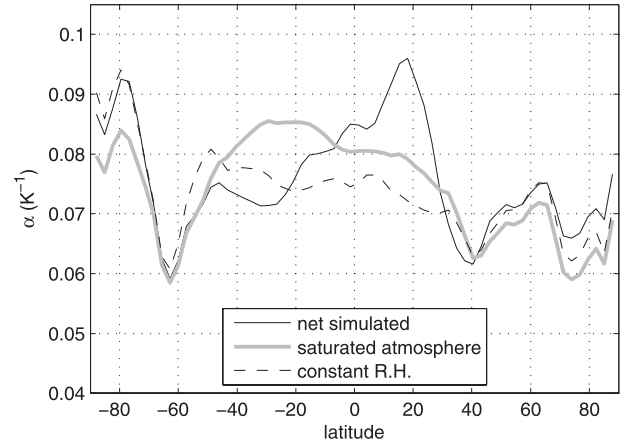


FIG. 3. The multimodel mean for all eight models in Table 1 of the zonal-mean rate of change of precipitable water computed by solving (3) for  $\bar{\alpha}$  using zonal-mean surface air temperature. The solid black line shows the total simulated change, the dashed line the change calculated assuming fixed relative humidity (i.e., modern relative humidities and LGM air temperatures), and the gray line a saturated atmosphere in both the modern and LGM.

specific humidity of the LGM models; the difference between this precipitable water distribution and the modern gives the change in  $W$  under a fixed relative humidity assumption. This distribution is shown by the dashed line in Fig. 3. For completeness, we also show the rate of change of  $W$  that would occur if the atmosphere was saturated in both the modern and LGM periods. This diagnostic assumption of a saturated atmosphere eliminates the height dependence of relative humidity that complicates vertical integration of (2), as discussed above; in the tropics and some of the subtropics this assumption of saturation produces rates of change of  $W$  slightly higher than those obtained under the constant relative humidity assumption, consistent with O’Gorman and Muller (2010). The rates of change calculated under the assumption of constant relative humidity are well within  $1\% \text{ K}^{-1}$  of the simulated change at all latitudes poleward of  $30^\circ$  in both hemispheres. In the tropics, especially the tropical Northern Hemisphere, the rate of change is higher than that expected under the assumption of fixed relative humidity. Given that  $\Delta T_s$  is negative, this means that the relative humidity of the tropical atmosphere is lower in the LGM than in the modern simulations, at least at levels containing the bulk of column water vapor.

This super-Clausius–Clapeyron reduction in tropical precipitable water is associated with lower-tropospheric relative humidities that change at a rate of about 0.5% per degree change in global-mean surface air temperature (Fig. 4). Since simulated global-mean surface air temperature was 3–6 K lower in the LGM than in the

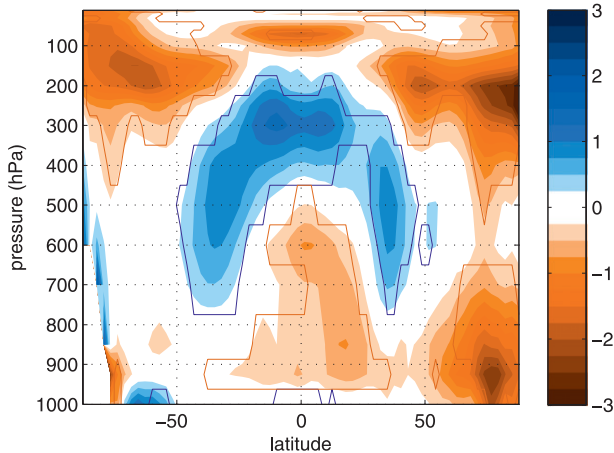


FIG. 4. Multimodel-mean rate of change of zonal-mean relative humidity, normalized by the absolute value of global-mean surface air temperature change for each model so units are  $\% \text{ K}^{-1}$ . Red shading denotes humidities that were lower in the LGM, blue shading humidities higher in the LGM, and regions inside solid lines are significantly different from zero in the multimodel mean using a two-tailed Student's  $t$  test at a 0.05 level. Includes data from all eight models in Table 1.

modern period, simulated tropical lower-tropospheric relative humidities thus fall by a total of only a few percent. In Fig. 4, we normalized the change in relative humidity by the absolute value of the change in global-mean surface air temperature for each model before computing the multimodel mean to reduce intermodel spread caused only by the magnitude of global-mean cooling. This normalization also allows changes in relative humidity to be directly compared with estimates of  $\bar{\alpha}$ , so that the latter can be seen to be about an order of magnitude larger. Note that, near  $20^\circ\text{N}$ , a relative humidity change peaking near  $1\% \text{ K}^{-1}$  at 850 hPa corresponds to an increase in  $\bar{\alpha}$  about  $2\% \text{ K}^{-1}$  beyond the value expected under the assumption of constant relative humidity. This difference between  $\bar{\alpha}$  and the change in relative humidity is consistent with that expected for concurrent changes in relative humidity and temperature along a moist adiabat.<sup>3</sup> Because of the nonlinearity of the Clausius–Clapeyron relation, inhomogeneities in both the zonal and seasonal distributions of temperature change may also play a role in producing rates of change

of  $W$  that exceed those expected at constant relative humidity. Normalization by global-mean instead of zonal-mean temperature change inflates the change in relative humidity at high latitudes, which is why the large changes in lower-tropospheric Arctic relative humidity in Fig. 4 are not accompanied by enhanced  $\bar{\alpha}$  in Fig. 3.

In contrast to lower-tropospheric relative humidities, upper-tropospheric relative humidities increase about  $0.5\% \text{ K}^{-1}$  in the tropics and subtropics, and relative humidities near and above the tropopause decrease (Fig. 4). These patterns are similar to those discussed for simulations of next-century warming, up to the expected sign change (e.g., Mitchell and Ingram 1992; Lorenz and DeWeaver 2007; Sherwood et al. 2010a; Wright et al. 2010). We do not delve into detailed explanations for this characteristic pattern of change in zonal-mean relative humidity because it makes what will be shown (in the next section) to be a negligible contribution to changes in  $P - E$ , and because some possible mechanisms have been discussed in those previous works.

## 5. Changes in $P - E$

### a. Overview

The previous section showed that simulated changes in  $W$  between the LGM and modern are approximately consistent with the assumption of fixed lower-tropospheric relative humidity, with some deviation in the Northern Hemisphere tropics (Fig. 3). In this section we examine whether the thermodynamic scaling for  $P - E$  predicated on this assumption provides a decent approximation to changes simulated in the PMIP2 models.

We begin by examining the rate of change of global-mean  $P$  relative to global-mean  $T_s$  across the ensemble of PMIP2 models, as was done for  $W$  in the previous section. The Clausius–Clapeyron relation places no constraint on changes in global-mean  $P$ . Instead, any change in global-mean  $P$  must be balanced by the same change in global-mean  $E$ , and the latter is constrained to some degree by the surface energy budget (e.g., Boer 1993). Global-mean  $E$  does increase in simulations of next-century warming, but does so at a comparatively low rate near  $2\% \text{ K}^{-1}$  due to changes in the Bowen ratio, net surface longwave radiation, clouds, and other factors (Held and Soden 2006). In the PMIP2 models, global-mean  $P$  changes at a similar rate of about  $2\% \text{ K}^{-1}$  between the simulated LGM and modern climates (Fig. 1a), where this rate of change was computed using the same logarithmic formula employed for column water vapor [i.e.,  $\bar{\alpha} = \log(P_{\text{LGM}}/P_{\text{mod}})/\Delta T_s$ ]. Unlike our calculation for  $W$ , we show rates of change of  $P$  only for the method where the global mean was taken before the ratio and logarithm because reversing that order of operations

<sup>3</sup> An example calculation shows that, assuming a moist pseudoadiabat and an idealized relative humidity profile with a mid-tropospheric minimum, a decrease in surface temperature from  $25^\circ$  to  $24^\circ\text{C}$  at constant relative humidity produces a change in precipitable water of 8.0%, while the same temperature change with a concurrent decrease in relative humidity of 1% at all levels produces a precipitable water change of 9.8%; thus, a change in relative humidity of 1% enhances  $\bar{\alpha}$  by 1.8%.

entails division by very small numbers in regions where precipitation approaches zero. Since there is no theoretical scaling with which to compare the simulated rate of change of global-mean  $P$ , the fact that the calculation presented in Fig. 1a may be biased is of little consequence; the important point is that it is considerably lower than the rate of change of  $W$ .

The horizontal distribution of  $P$  in simulations of the LGM has been examined by previous authors, who emphasized a global-scale reduction in  $P$  compared to modern times, with the caveat that some midlatitude regions in both hemispheres receive more annual-mean precipitation (e.g., Braconnot et al. 2007). Here we are interested in the distribution of  $P - E$  rather than that of  $P$  alone, since we have a theoretical scaling for the former. The quantity  $P - E$  may also be a better measure of surface water availability, more directly related to quantities like glacial lake levels, vegetation, and the aridity of dust source regions (e.g., Farrera et al. 1999; McGee et al. 2010). It is thus worth noting that, compared to modern times, the LGM simulations are characterized by large regions of enhanced  $P - E$  in the subtropics (Fig. 5, where we again normalized each model by the absolute value of its global-mean surface air temperature change before taking the multimodel mean). These regions of enhanced  $P - E$  in the LGM are more horizontally extensive than the region of enhanced  $P$ , consistent with the fact that changes in  $E$  are much more horizontally uniform and are negative nearly everywhere (not shown), as expected for global cooling. In particular, note the difference in sign between  $\delta(P - E)$  and  $\delta P$  over large parts of both North America and all subtropical ocean basins. The only location in the PMIP2 simulations where  $E$  increased on large scales was the North Atlantic, seemingly due to the eastward flow of extremely cold and dry air from the Laurentide ice sheet and Labrador Sea (Hewitt et al. 2003; Shin et al. 2003).

#### b. Evaluation of thermodynamic scaling

Now we present a more quantitative analysis of the simulated changes in  $P - E$ . To calculate all terms in (7) one needs  $\mathbf{F}$  as well as  $P - E$ , and unfortunately the former is archived by far fewer modeling groups than the latter. For this reason we first compare the zonal-mean distributions of  $\delta(P - E)$  in the full ensemble of models with  $\bar{\alpha}\delta T(P - E)$ , then examine the more complete thermodynamic estimate of  $\delta(P - E)$ , given by (7), in the two models for which  $\mathbf{F}$  is available. Before computing multimodel means, all quantities are normalized by the absolute value of global-mean surface air temperature change for each model.

Simulated zonal-mean  $P - E$  was lower in the tropics during the LGM, higher in the subtropics, and lower in

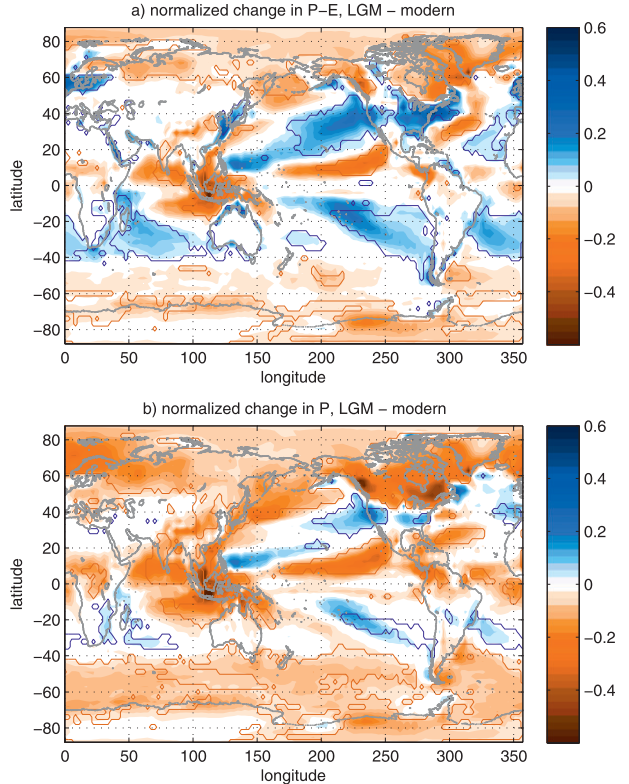


FIG. 5. Multimodel-mean rate of change of (a) precipitation minus surface evaporation and (b) precipitation, normalized by the absolute value of global-mean surface air temperature change for each model so the units are  $\text{mm day}^{-1} \text{K}^{-1}$ . Red shading denotes quantities lower in the LGM, blue shading quantities higher in the LGM, and regions inside solid lines are significantly different from zero in the multimodel mean using a two-tailed Student's  $t$  test at a 0.05 level. Includes data from all eight models in Table 1.

high latitudes (Fig. 6). The first term on the right-hand side of (7), calculated using data from all models for which  $P - E$  was available using the global-mean value of  $\bar{\alpha} = 7.7\% \text{ K}^{-1}$ , is given by the dashed line in Fig. 6. Although this partial thermodynamic scaling under-predicts the meridional width of the subtropical moistening and greatly overpredicts the magnitude of high-latitude drying, it provides a decent quantitative match in the deep tropics and a rough qualitative match elsewhere, at least in the zonal mean. There are differences in zonal-mean  $P - E$  distributions between the individual PMIP2 models (shown by the gray lines in Fig. 6), but they all exhibit higher  $P - E$  in the subtropics and lower  $P - E$  in both the tropics and high latitudes. The high-amplitude outlier in which  $P - E$  is enhanced by  $0.2 \text{ mm day}^{-1} \text{ K}^{-1}$  near  $50^\circ$  latitude in each hemisphere is the FGOALS-g1.0 model, which has weak poleward ocean heat transport and overestimates sea ice by a factor of two in the modern climate [Zhang and Walsh (2006), and the Coupled Model Intercomparison Project phase 3 (CMIP3) documentation].

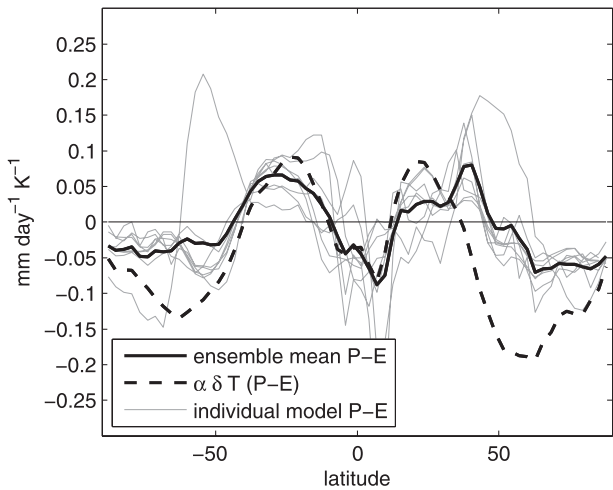


FIG. 6. Zonal-mean rate of change of precipitation minus surface evaporation normalized by the absolute value of global-mean surface air temperature change for each model so units are  $\text{mm day}^{-1} \text{K}^{-1}$ . Thin gray lines are results for each model in Table 1, the thick solid line the multimodel mean, and the dashed line is the thermodynamic estimate using the first term on the right-hand side of (7).

There are large zonal asymmetries in simulated  $\delta(P - E)$ , as seen in the multimodel mean shown in Fig. 5a and in the mean of the two models for which  $\mathbf{F}$  is available (Fig. 7a; note the change in color scale between these two figures). The subtropical increase in  $P - E$  is part of a pattern of tilted bands of anomalous  $P - E$  that stretch from the western tropics of each ocean basin to the eastern subtropics. One of the most prominent bands stretches from the tropical western Pacific to the east coast of North America, where  $P - E$  is enhanced over the entirety of what is now the conterminous United States. The thermodynamic scaling that neglects the second term on the right-hand side of (7) quite dramatically underpredicts the intensity and meridional width of these regions of subtropical increase in  $P - E$ , and even gives the wrong sign for  $\delta(P - E)$  over much of North America and Europe (Fig. 7b). The agreement between the zonal-mean values of  $\delta(P - E)$  and  $\bar{\alpha}\delta T(P - E)$  in the deep tropics occurs because of cancellation between regions of strong increase and decrease of  $P - E$  at the same latitude. These zonal asymmetries are stronger than those exhibited in simulations of next-century warming, where the subtropical decrease in  $P - E$  occurs in zonal bands that are oriented much more in the pure east–west direction (e.g., Fig. 7 of Held and Soden 2006).

The second term on the right-hand side of (7) has a much larger amplitude than the first term in most of the extratropics, even in regions not adjacent to ice sheets (Fig. 7c). This shows that a strong increase in  $P - E$  over

much of North America during the LGM is consistent with strong horizontal temperature gradients south and west of the Laurentide ice sheet. In this context,  $\bar{\alpha}\mathbf{F} \cdot \nabla(\delta T)$  represents enhanced moisture convergence occurring as saturation humidity drops when winds blow from oceanic regions undergoing relatively little temperature change onto cold, high ice sheets. Note that this term does not separate condensation due to ascent over orography from condensation due to winds blowing into a colder region; because saturation vapor pressure depends only on temperature and not total air pressure, this provides a crude way of including the effects of anomalous forced orographic ascent.

The sum of both terms on the right-hand side of (7) produces a pattern that is dominated by  $\bar{\alpha}\delta T(P - E)$  in the tropics and by  $\bar{\alpha}\mathbf{F} \cdot \nabla\delta T$  in the extratropics (Fig. 7d). This thermodynamic scaling deviates considerably from the simulated  $\delta(P - E)$  in many regions, predicting a larger increase in  $P - E$  over the western part of North America and a larger decrease over its northeastern coast. The simulated increases in  $P - E$  across the entire width of the Pacific Ocean are underestimated in both amplitude and horizontal extent, as is the decrease in  $P - E$  over Indonesia. In summary, while the part of the thermodynamic scaling typically used for next-century warming provides a qualitative match to the change in  $P - E$  in the zonal mean, it provides a poor estimate of the patterns and amplitude of regional change. The additional term accounting for changes in horizontal temperature gradients dominates the complete thermodynamic estimate in the extratropics, but does not produce even a decent qualitative match to the regional patterns of hydrological change.

Given that  $\bar{\alpha}$  does change from about 10% to 6%  $\text{K}^{-1}$  over 20° of latitude (Fig. 3), it seems reasonable to ask whether some of the mismatch between the simulated distribution of  $\delta(P - E)$  and the thermodynamic estimate might result from neglecting gradients of  $\bar{\alpha}$ . For this reason, we calculated the right-hand side of (6) using the zonal-mean value of  $\bar{\alpha}$  from each model, together with the full horizontal distributions of  $\delta T$  and  $\mathbf{F}$ . As discussed above, we do not calculate  $\bar{\alpha}$  as a function of both latitude and longitude because this distribution is extremely noisy because of the existence of regions where  $\delta T$  changes sign. The result of this calculation shows that horizontal variations in  $\bar{\alpha}$  make a negligible contribution to the thermodynamic scaling for changes in  $P - E$  (cf. Fig. 8 with Fig. 7d).

### c. Dynamical changes

Since the thermodynamic scaling does not provide a decent approximation to simulated  $\delta(P - E)$  as a function of latitude and longitude, dynamical changes

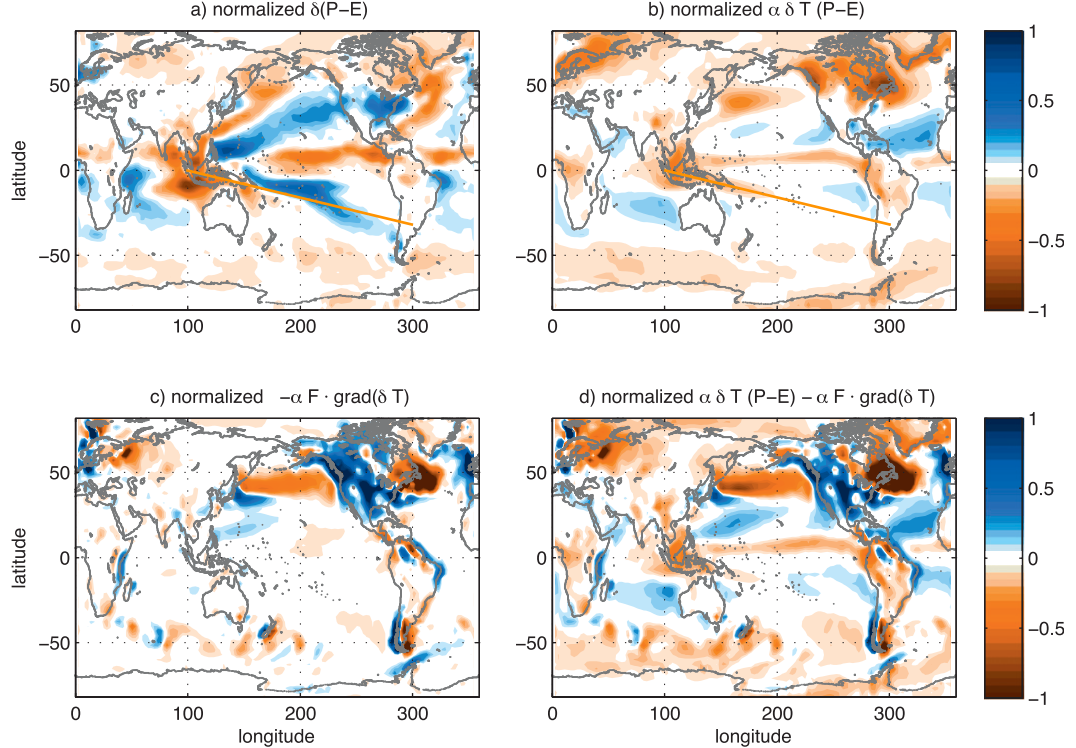


FIG. 7. As in Fig. 5, but for the two models for which moisture fluxes were available. (a) The simulated change in  $P - E$  for those models; (b) the thermodynamic estimate using the first term on the right-hand side of (7); (c) the second term on the right-hand side of (7); and (d) the sum of both terms on the right-hand side of (7). Statistically significant regions are not shown because there are results for only two models.

[i.e., changes in  $\mathbf{v}$  in (5)] seem a likely cause of this deviation. Multiple candidate dynamical mechanisms exist. Relative to modern climate, LGM models exhibit a strengthening and meridional contraction of the Hadley circulation (Murakami et al. 2008; Ganopolski et al. 1998). However, deviations from the thermodynamic scaling exhibit high-amplitude zonal asymmetries that cannot be explained in terms of changes in zonally symmetric Hadley transports. Large changes in continental and sea ice modified the extratropical flow, especially the Northern Hemisphere storm tracks (Broccoli and Manabe 1987; Hall et al. 1996; Justino et al. 2005; Laîné et al. 2009). Since the moisture flux carried by transient eddies dominates the extratropical hydrological cycle in the present climate (Peixoto and Oort 1992), it would not be surprising if these extratropical dynamical changes produced deviations from a purely thermodynamic scaling for  $P - E$ . However, deviations from the thermodynamic scaling extend deep into the tropics, making any connection to extratropical eddies far from obvious. So to help attribute  $\delta(P - E)$  to a particular category of dynamical change, we decompose the changes in  $P - E$  into changes associated with transient eddies, stationary eddies, and the mean meridional circulation.

We use a standard eddy decomposition (e.g., Peixoto and Oort 1992) where an overbar and prime (e.g.,  $\bar{q}, q'$ ) denote the time mean and anomalies from that mean, and brackets and stars (e.g.,  $[q], q^*$ ) denote the zonal mean and anomalies from that mean, respectively. The mass-weighted, vertically integrated northward atmospheric moisture transport can then be written as follows:

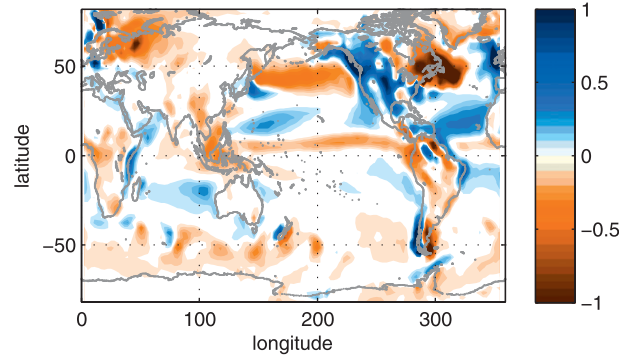


FIG. 8. As in Fig. 7b, but for the thermodynamic estimate computed using the right-hand side of (6).

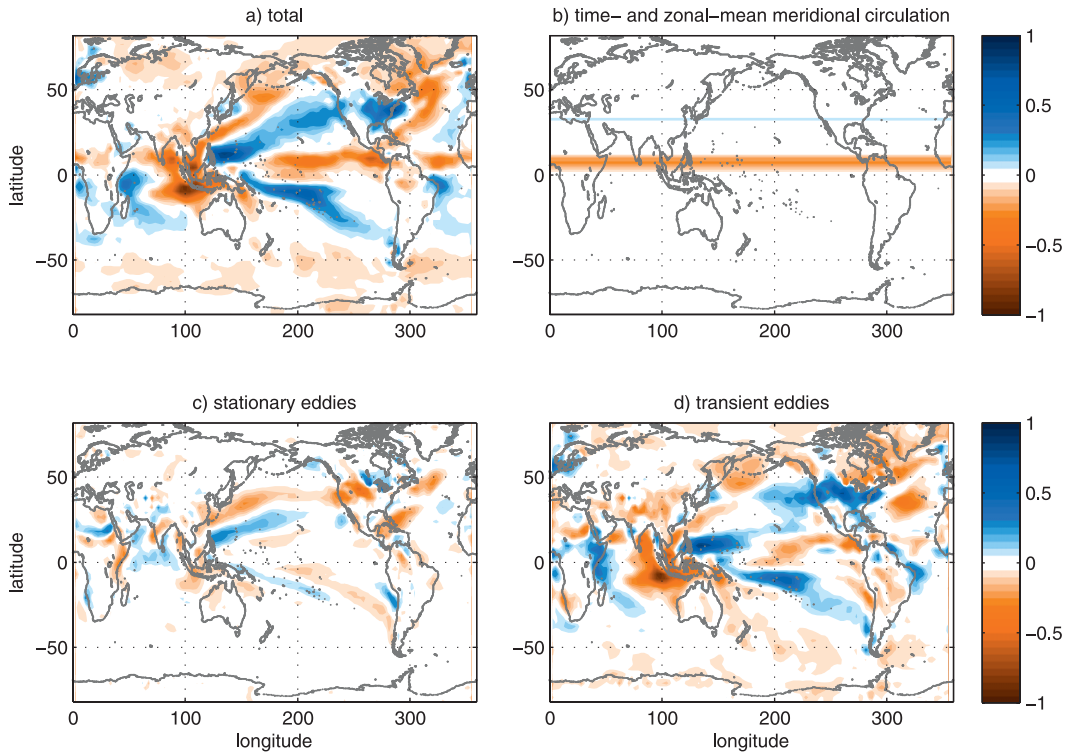


FIG. 9. Decomposition of the change in precipitation minus evaporation into parts associated with eddies and mean flow for the two models for which moisture fluxes were available. The LGM–modern vertically integrated moisture flux convergence due to (a) all motions, (b) the time- and zonal-mean meridional circulation, (c) stationary eddies, and (d) transient eddies. All quantities are normalized by the absolute value of global-mean surface air temperature change for each model, so units are  $\text{mm day}^{-1} \text{K}^{-1}$ .

$$\int [\bar{v}\bar{q}] dp = \int [\bar{q}][\bar{v}] dp + \int [\bar{q}^*\bar{v}^*] dp + \int [\bar{q}'\bar{v}'] dp, \quad (8)$$

where all integrals are evaluated from the surface to the top of the atmosphere and we have omitted the factor of  $1/g$ . The terms on the right-hand side represent, respectively, transports by the mean meridional circulation (MMC), stationary eddies, and transient eddies. In practice we compute the first two terms on the right-hand side from vertically resolved time-mean values of  $v$  and  $q$ . The left-hand side is simply the northward component of the vertically integrated moisture flux  $\mathbf{F}$  discussed above; because this is available for only two of the models in Table 1, this analysis is again conducted for only those models. We compute the transient eddy contribution (the last term on the right-hand side) as a residual because daily, vertically-resolved values of  $v$  and  $q$  are not part of the PMIP2 archive. Before computing multimodel means, all quantities are normalized by the absolute value of global-mean surface air temperature change for each model. Since the convergence of this vertically integrated moisture transport must balance  $P - E$ , we can take the horizontal convergence

of (8) and associate each term on the right-hand side with a contribution to the total  $P - E$  by the MMC, stationary eddies, and transient eddies. It is important to note that each term in (8) will include changes in moisture transports due to both dynamics and thermodynamics. While we could separate the dynamic and thermodynamic changes (e.g., Seager et al. 2010), this is a fairly lengthy task and here we simply show which term on the right-hand side of (8) dominates the total, knowing from results presented above that the thermodynamic change provide a poor approximation to the total.

The contribution of each term in (8) to  $\delta(P - E)$  is displayed in Fig. 9. The change in convergence of total moisture transports [i.e., the left-hand side of (8)] is nearly identical to the explicitly calculated  $\delta(P - E)$  displayed in Fig. 7a. This confirms that the moisture budget is closed and no large errors were introduced by calculation of horizontal divergence in a coordinate different from the native model system. Changes in transient eddy transports produce most of the total change in  $P - E$  while changes associated with the MMC and stationary eddies are comparatively weak. Although the total mass flux in the Hadley circulation is stronger in the LGM than

in the modern period (not shown), the reduction in precipitable water (i.e., the thermodynamic change) overcompensates so that the total change in moisture transports associated with the MMC produces a near-equatorial decrease in  $P - E$ . This decrease accounts for much of the reduction in  $P - E$  in the tropical Atlantic and the central and eastern Pacific but is otherwise small compared to changes associated with eddy transports. This is an important point: most of the subtropical increase in  $P - E$  in the LGM cannot be thought of as being directly produced by zonally symmetric changes in Hadley circulation transports.

Stationary eddies enhance  $P - E$  in tilted bands across the Pacific, but these are weak compared to the total change. Stationary eddies also reduce  $P - E$  over western North America, opposing the stronger increase associated with transient eddies. While it might be physically reasonable to expect the enhanced stationary wave produced by the Laurentide ice sheet (e.g., Cook and Held 1988) to diverge moisture out of this region, a detailed study of the dynamical influence of stationary waves on the moisture field is outside the scope of this study.

The highest-amplitude changes associated with transient eddies occur over midlatitude North America and within  $20^\circ$  of the equator in the Indian and Pacific Oceans. The North American changes are likely caused by the Laurentide ice sheet and resemble those due to thermodynamic changes associated with strong increases in horizontal temperature gradients [i.e., the last term in (7) and Fig. 7c]. In other words, much of the transient eddy contribution to  $\delta(P - E)$  over North America may be thermodynamic, resulting from moisture condensing as it is advected in transient eddies from an oceanic region experiencing little temperature change to an ice sheet where temperature drops dramatically. The transient eddy field itself surely changed in association with a southward shift in Northern Hemisphere storm tracks (e.g., Kageyama et al. 1999), making an additional dynamical contribution to  $\delta(P - E)$ .

The cause of the tropical changes in  $P - E$  associated with transient eddies is unclear but may be related to changes in the Walker circulation. Modern peak precipitation in the Indo-Pacific region is centered over the equator near  $110^\circ\text{E}$  (as can be inferred from Fig. 7b), so the east–west dipole in  $\delta(P - E)$  in this region corresponds to an eastward shift in that precipitation peak. It is unclear why the changes in  $P - E$  peak off the equator, but the increase in the tropical South Pacific may be associated with an eastward extension of the South Pacific convergence zone (SPCZ). Although the Walker circulation is often thought of as a time-mean field, Vecchi and Soden (2007) showed that a weakening of the Walker circulation in simulations of greenhouse gas-induced

warming consisted of a reduction in the frequency of episodes of strong ascent over the western Pacific warm pool. The dominant tropical changes in  $P - E$  in the PMIP2 models may thus be associated with an eastward shift in episodic strong ascent in the warm-pool region. The simulated LGM changes in the eastern Pacific due to transient eddies are weak compared to those in the western Pacific, so it is unclear whether a strengthening of the Walker circulation occurs with anomalous East Pacific subsidence projecting onto the MMC changes or whether other dynamics are at play. DiNezio et al. (2011) argue that a general increase in Walker circulation strength in LGM simulations is complicated by a weakening of ascent over the Maritime Continent where additional land was exposed because of the glacial drop in sea level. While this is not inconsistent with results presented here, it does not explain the off-equatorial increase in  $P - E$  in the western and central Pacific. It is important to note that the increase in  $P - E$  in the western Pacific is weaker in the average across all eight models than in the two models for which vertically integrated moisture fluxes are available (cf. Fig. 5a with Fig. 7a), illustrating intermodel variability in these dynamical changes.

## 6. Implications for proxy selection and interpretation

The above results show that it is misleading, at best, to interpret climate proxy data for the LGM in a zonally symmetric context. While it may be tempting to think of  $P - E$  being enhanced in the subtropics during the LGM, analogous to the reduction in subtropical  $P - E$  expected for next-century warming, zonal asymmetries in the model response are sufficiently large so as to make such a zonal-mean picture of questionable utility when interpreting proxies at particular sites. Most of the subtropical increase in  $P - E$  simulated by the suite of models examined here occurs in poleward-tilted bands that stretch across ocean basins, while most proxies for hydrological change (e.g., lake extent, pollen counts, and sediment accumulation) primarily represent local changes over land. The picture is further complicated by the fact that the simulated increase in  $P - E$  occurring over much of North America and Europe can be accounted for by a thermodynamic scaling only by including the effects of large increases in horizontal temperature gradients near the edges of ice sheets in those regions, so that proxies in those regions cannot be expected to confirm or refute the thermodynamic theory used to describe next-century hydrological change (e.g., Held and Soden 2006). Over continents other than North America, the models exhibit changes in  $P - E$  that are of variable sign

and weak compared to oceanic changes, with the exception of high-latitude Asia (e.g., Fig. 5a). While it is possible that these continental changes can be reconciled with some global theory for the LGM hydrological cycle, it should be noted that outside of North America and northern Asia, even the stronger changes over Southeast Asia and northern Africa exhibit sufficient spread between the models so as to lie outside bounds of statistical significance in the multimodel mean (Fig. 5). This also raises the question of whether theory and models should be evaluated based on their agreement with observations in a region where any signal is expected to be relatively weak.

It is interesting that there are numerous regions where changes in  $P$  and  $P - E$  have opposite signs in the multimodel mean (e.g., Fig. 5). Thus, a proxy that is more sensitive to  $P - E$ , such as lake extent, may show an opposite change to a proxy that is more sensitive to  $P$ . Given this expected sign reversal between  $P$  and  $P - E$  in some regions, together with the relatively weak and inconsistent patterns of hydrological change over many subtropical land regions, it becomes apparent that using proxy data from subtropical continents to validate the behavior of LGM climate models is likely a subtle and difficult task. An exception, as stated above, is over North America and Europe, but all one might be verifying in those regions is the local response of  $P$  and  $P - E$  to the thermal and orographic forcing of ice sheets.

We do not mean to suggest that the effort to compare proxy data with models is futile but that care must be taken when selecting regions for comparison. It might be useful to conduct an experimental design process to determine optimal locations for validating the patterns of hydrological change simulated by PMIP2 models, but such a task is beyond the scope of this study. Instead, we suggest that effort be made to find and analyze proxy records in locations where changes in  $P$  and  $P - E$  are of high amplitude and perhaps also of consistent sign across models. This would provide a clear test of the dominant pattern of hydrological change simulated by the models. Also, selecting proxies in locations remote from LGM ice sheets is more likely to provide an observational constraint that is generally relevant to hydrological change in a range of climates and not specific to local changes induced by ice sheets.

## 7. Summary and conclusions

The first part of this paper showed that simulated changes in precipitable water between modern and LGM climates are well described by a scaling based on the assumption of invariant lower-tropospheric relative humidity. This is perhaps not surprising since a similar

set of climate models follows the same scaling as climate warms in response to enhanced greenhouse gas concentrations (e.g., Held and Soden 2006). Nevertheless, the result had not been previously demonstrated, and it was conceivable that the thermodynamic or orographic influence of LGM ice sheets could have unforeseen effects on simulated precipitable water. We showed that while there were small to moderate deviations from the assumption of constant lower-tropospheric relative humidity, these deviations had a negligible effect on the distribution of  $P - E$  (demonstrated by comparison of Fig. 8 with Fig. 7d). Furthermore, changes in the zonal-mean profile of relative humidity that did occur were similar, up to the expected sign change, to those seen in simulations of next-century warming. Explanations for relative humidity changes in next-century warming (e.g., Sherwood et al. 2010b; Wright et al. 2010) are thus likely relevant to LGM climate.

While no set of climate proxies may ever be found to strongly constrain distributions of relative humidity and precipitable water during the LGM, examining theoretical and numerical estimates of these quantities is important because they form part of a theory for how  $P - E$  changes with temperature. A simple scaling based on the assumptions of fixed circulation and fixed relative humidity was previously shown to provide a decent description of simulated changes of next-century  $P - E$ , both in the zonal mean and as a function of latitude and longitude (e.g., Held and Soden 2006). Dynamical changes (e.g., in the strength and meridional width of the Hadley circulation) do modify  $P - E$  but are not so large that they alter the qualitative agreement between the thermodynamic scaling and simulations of next-century warming. In contrast, a thermodynamic scaling does not describe changes in  $P - E$  between the LGM and modern climates nearly as well. While the scaling did provide a qualitative estimate of simulated  $\delta(P - E)$  between the LGM and modern periods in the zonal mean, this agreement was shown to result from the cancellation of strong positive and negative changes at the same latitude. The simulated subtropical change in  $P - E$  had much more of a north-south tilt in the LGM simulations than in patterns previously published for next-century warming (e.g., Fig. 7 of Held and Soden 2006). The thermodynamic scaling thus seems to have little descriptive power for regional change, making it of questionable use for interpreting proxies for LGM precipitation and surface evaporation. We did find that an additional term in the thermodynamic scaling that linearly relates changes in  $P - E$  to changes in horizontal temperature gradients is important for the LGM and dominates the complete thermodynamic scaling in the extratropics. But even accounting for these

gradients in temperature change in the scaling produced a poor estimate of the simulated  $P - E$  field.

Since the fixed-relative humidity assumption of the scaling was shown to hold in the models, violation of the other assumption of fixed circulation is a likely explanation for deviations from the thermodynamic scaling. Previous work has indeed shown that LGM climate models predict a strengthening and meridional contraction of the Hadley circulation (e.g., Murakami et al. 2008). However, our decomposition of the total change in  $P - E$  into parts associated with transient eddies, stationary eddies, and zonal-mean meridional circulation showed that changes in zonally symmetric Hadley circulation transports make a relatively minor contribution. Changes due to transient eddies dominate and have the highest amplitude over North America and in the tropical western Pacific/Indonesian region. Over North America these transient eddy changes might be associated with the southward shift of the jet stream and storm track (Lainé et al. 2009), while in the western Pacific they may be associated with changes in the Walker circulation (DiNezio et al. 2011). It is unclear whether it is a coincidence that tilted bands of  $\delta(P - E)$  are consistently simulated in the Indian, Pacific, and Atlantic oceans in both hemispheres or whether some greater mechanism is at work. This equatorial symmetry is especially puzzling since LGM climate models show disparate changes in the strength and location of the Southern Hemisphere westerly jet (Rojas et al. 2009). We leave a more complete investigation of dynamically induced changes in the LGM hydrological cycle for separate work.

The results presented here suggest that changes in the LGM hydrological cycle may be better described in terms of dynamical changes than in terms of a purely thermodynamic scaling. This implies that LGM climate proxies are likely ill-suited to serve as an observational test for the thermodynamic scaling shown to describe simulated next-century hydrological change (e.g., Held and Soden 2006). That scaling may hold in the next century, but dynamical changes in moisture transports may be large enough between LGM and modern climates that the LGM cannot be thought of as a cold analog for the hydrological changes associated with next-century warming.

**Acknowledgments.** This work was partly supported by the Comer Science and Education Foundation. Conversations with Wallace Broecker motivated this work, and David McGee, Tim Merlis, Paul O’Gorman, and three anonymous reviewers provided helpful comments. We acknowledge the international modeling groups for providing their data for analysis and the Laboratoire des Sciences du Climat et de l’Environnement (LSCE) for collecting and archiving the model data. The PMIP2

Data Archive is supported by CEA, CNRS, the EU project MOTIF (EVK2-CT-2002-00153) and the Programme National d’Etude de la Dynamique du Climat (PNEDC). The analyses were performed using version 01-20-2010 of the database. More information is available online at <http://pmip2.lsce.ipsl.fr>.

## REFERENCES

- Allen, M., and W. Ingram, 2002: Constraints on future changes in the hydrological cycle. *Nature*, **419**, 224–228.
- Berger, A., 1978: Long-term variations of caloric insolation resulting from the earth’s orbital elements. *Quat. Res.*, **9**, 139–167.
- Boer, G., 1993: Climate change and the regulation of the surface moisture and energy budgets. *Climate Dyn.*, **8**, 225–239.
- Bolton, D., 1980: The computation of equivalent potential temperature. *Mon. Wea. Rev.*, **108**, 1046–1053.
- Braconnot, P., and Coauthors, 2007: Results of PMIP2 coupled simulations of the mid-Holocene and last glacial maximum—Part 1: Experiments and large-scale features. *Climate Past*, **3**, 261–277.
- Broccoli, A., 2000: Tropical cooling at the last glacial maximum: An atmosphere–mixed layer ocean model simulation. *J. Climate*, **13**, 951–976.
- , and S. Manabe, 1987: The influence of continental ice, atmospheric CO<sub>2</sub>, and land albedo on the climate of the last glacial maximum. *Climate Dyn.*, **1**, 87–99.
- Chou, C., and J. Neelin, 2004: Mechanisms of global warming impacts on regional tropical precipitation. *J. Climate*, **17**, 2688–2701.
- Cook, K., and I. Held, 1988: Stationary waves of the ice age climate. *J. Climate*, **1**, 807–819.
- DiNezio, P., A. Clement, G. Vecchi, B. Soden, A. J. Broccoli, B. Otto-Btiesner, and P. Braconnot, 2011: The response of the Walker circulation to Last Glacial Maximum forcing: Implications for detection in proxies. *Paleoceanography*, **26**, PA3217, doi:10.1029/2010PA002083.
- Emori, S., and S. Brown, 2005: Dynamic and thermodynamic changes in mean and extreme precipitation under changed climate. *Geophys. Res. Lett.*, **32**, L17706, doi:10.1029/2005GL023272.
- Farrera, I., and Coauthors, 1999: Tropical climates at the last glacial maximum: A new synthesis of terrestrial palaeoclimate data. I: Vegetation, lake-levels, and geochemistry. *Climate Dyn.*, **15**, 823–856.
- Ganopolski, A., S. Rahmstorf, V. Petoukhov, and M. Claussen, 1998: Simulation of modern and glacial climates with a coupled global model of intermediate complexity. *Nature*, **391**, 351–356.
- Hall, N., P. Valdes, and B. Dong, 1996: The maintenance of the last great ice sheets: A UGAMP GCM study. *J. Climate*, **9**, 1004–1019.
- Hargreaves, J., A. Abe-Ouchi, and J. Annan, 2007: Linking glacial and future climates through an ensemble of GCM simulations. *Climate Past*, **3**, 77–87.
- Held, I., and B. Soden, 2000: Water vapor feedback and global warming. *Annu. Rev. Energy Environ.*, **25**, 441–475.
- , and —, 2006: Robust responses of the hydrological cycle to global warming. *J. Climate*, **19**, 5686–5699.
- Hewitt, C., R. Stouffer, A. Broccoli, J. Mitchell, and P. Valdes, 2003: The effect of ocean dynamics in a coupled GCM simulation of the last glacial maximum. *Climate Dyn.*, **20**, 203–218.

- Joussaume, S., and K. Taylor, 1995: Status of the Paleoclimate Modeling Intercomparison Project. *Proc. First Int. AMIP Scientific Conf.*, Monterey, CA, World Meteorological Organization, 425.
- Justino, F., A. Timmermann, U. Merkel, and E. Souza, 2005: Synoptic reorganization of atmospheric flow during the last glacial maximum. *J. Climate*, **18**, 2826–2846.
- Kageyama, M., P. Valdes, G. Ramstein, C. Hewitt, and U. Wyputta, 1999: Northern Hemisphere storm tracks in present day and last glacial maximum climate simulations: A comparison of the European PMIP models. *J. Climate*, **12**, 742–760.
- Kutzbach, J., J. Williams, and S. Vavrus, 2005: Simulated 21st century changes in regional water balance of the Great Lakes region and links to changes in global temperature and poleward moisture transport. *Geophys. Res. Lett.*, **32**, L17707, doi:10.1029/2005GL023506.
- Laîné, A., and Coauthors, 2009: Northern Hemisphere storm tracks during the last glacial maximum in the PMIP2 ocean-atmosphere coupled models: Energetic study, seasonal cycle, precipitation. *Climate Dyn.*, **32**, 593–614.
- Lorenz, D., and E. DeWeaver, 2007: The response of the extratropical hydrological cycle to global warming. *J. Climate*, **20**, 3470–3484.
- McGee, D., W. Broecker, and G. Winckler, 2010: Gustiness: The driver of glacial dustiness? *Quat. Sci. Rev.*, **29**, 2340–2350.
- Meehl, G., and Coauthors, 2007: Global climate projections. *Climate Change 2007: The Physical Science Basis*, S. Solomon et al., Eds., Cambridge University Press, 747–845.
- Mitchell, J., and W. Ingram, 1992: Carbon dioxide and climate: Mechanisms of changes in cloud. *J. Climate*, **5**, 5–21.
- Murakami, S., R. Ohgaito, A. Abe-Ouchi, M. Crucifix, and B. Otto-Bliesner, 2008: Global-scale energy and freshwater balance in glacial climate: A comparison of three PMIP2 LGM simulations. *J. Climate*, **21**, 5008–5033.
- O’Gorman, P., and T. Schneider, 2008: The hydrological cycle over a wide range of climates simulated with an idealized GCM. *J. Climate*, **21**, 3815–3832.
- , and C. Muller, 2010: How closely do changes in surface and column water vapor follow Clausius–Clapeyron scaling in climate change simulations? *Environ. Res. Lett.*, **5**, 025207, doi:10.1088/1748-9326/5/2/025207.
- Peixoto, J. P., and A. H. Oort, 1992: *Physics of Climate*. American Institute of Physics, 520 pp.
- Peltier, W., 2004: Global glacial isostasy and the surface of the ice-age Earth: The ICE-5G (VM2) model and GRACE. *Annu. Rev. Earth Planet. Sci.*, **32**, 111–149.
- Pierrehumbert, R., H. Brogniez, and R. Roca, 2007: On the relative humidity of the atmosphere. *The Global Circulation of the Atmosphere*, T. Schneider and A. H. Sobel, Eds., Princeton University Press, 143–185.
- Quade, J., and W. Broecker, 2009: Dryland hydrology in a warmer world: Lessons from the last glacial period. *Eur. Phys. J. Spec. Top.*, **176**, 21–36.
- Ramstein, G., Y. Serafini-Le Treut, H. Le Treut, M. Forichon, and S. Joussaume, 1998: Cloud processes associated with past and future climate changes. *Climate Dyn.*, **14**, 233–247.
- Rind, D., 1998: Latitudinal temperature gradients and climate change. *J. Geophys. Res.*, **103** (D6), 5943–5971.
- Rojas, M., and Coauthors, 2009: The southern westerlies during the last glacial maximum in PMIP2 simulations. *Climate Dyn.*, **32**, 525–548.
- Schneider, T., P. O’Gorman, and X. Levine, 2010: Water vapor and the dynamics of climate changes. *Rev. Geophys.*, **48**, RG3001, doi:10.1029/2009RG000302.
- Seager, R., N. Naik, and G. Vecchi, 2010: Thermodynamic and dynamic mechanisms for large-scale changes in the hydrological cycle in response to global warming. *J. Climate*, **23**, 4651–4668.
- Sherwood, S. C., W. Ingram, Y. Tsushima, M. Satoh, M. Roberts, P. Vidale, and P. O’Gorman, 2010a: Relative humidity changes in a warmer climate. *J. Geophys. Res.*, **115**, D09104, doi:10.1029/2009JD012585.
- , R. Roca, T. M. Weckwerth, and N. G. Andronova, 2010b: Tropospheric water vapor, convection, and climate. *Rev. Geophys.*, **48**, RG2001, doi:10.1029/2009RG000301.
- Shin, S., Z. Liu, B. Otto-Bliesner, E. Brady, J. Kutzbach, and S. Harrison, 2003: A simulation of the last glacial maximum climate using the NCAR-CCSM. *Climate Dyn.*, **20**, 127–151.
- Street-Perrott, F., and S. Harrison, 1985: Lake levels and climate reconstruction. *Paleoclimate Analysis and Modeling*, A. D. Hecht, Ed., John Wiley and Sons, 291–340.
- Trenberth, K., A. Dai, R. Rasmussen, and D. Parsons, 2003: The changing character of precipitation. *Bull. Amer. Meteor. Soc.*, **84**, 1205–1217.
- Vecchi, G., and B. Soden, 2007: Increased tropical Atlantic wind shear in model projections of global warming. *Geophys. Res. Lett.*, **34**, L08702, doi:10.1029/2006GL028905.
- Winkler, M., and P. Wang, 1993: The late-Quaternary vegetation and climate of China. *Global Climates Since the Last Glacial Maximum*, J. H. E. Wright et al. Eds., University of Minnesota Press, 221–264.
- Wright, J., A. Sobel, and J. Galewsky, 2010: Diagnosis of zonal mean relative humidity changes in a warmer climate. *J. Climate*, **23**, 4556–4569.
- Yoshimori, M., T. Yokohata, and A. Abe-Ouchi, 2009: A comparison of climate feedback strength between CO<sub>2</sub> doubling and LGM experiments. *J. Climate*, **22**, 3374–3395.
- Zhang, X., and J. Walsh, 2006: Toward a seasonally ice-covered Arctic Ocean: Scenarios from the IPCC AR4 model simulations. *J. Climate*, **19**, 1730–1747.